Hierarchical-Porous Copper Foams by a Combination of Sponge Replication and Freezing Techniques

Alina Sutygina,* Ulf Betke, and Michael Scheffler

Open-porous copper foams with additional strut porosity are manufactured by two different manufacturing routes. The first is based on the Schwarzwalder sponge replication technique. The second method is a combination of Schwartzwalder sponge replication and freezing technique in which an additional strut porosity is generated inside the struts of the sponge-replicated foams by freezing at −20 °C for 24 h and subsequent sublimation. Thermal processing of both types of foams is conducted at 500 and 900 °C for 6 h in a hydrogen-containing atmosphere to reduce copper oxides and to facilitate the sintering process of the copper powder particles. Despite significant shrinkage of both foam series after thermal processing, hollow struts and lamellar pores keep their shape and do not collapse. The influences of the additional lamellar pores and thermal processing temperature on the cellular structure, porosity, specific surface area, yield strength, absorbed energy, and thermal conductivity are studied. The additional strut porosity generated by the freezing step significantly increases the specific surface area of the copper foams by a factor of 2 in comparison to the sponge replicated foams.

1. Introduction

Copper foams have generated recent interest in energy devices, rechargeable batteries, heat exchangers, heat pumps, or fuel cells, due to a combination of a high thermal/electrical conductivity and a large specific surface area.[1–3] There are numerous methods to manufacture copper foams such as the space-holder technique by lost carbonate sintering processing,[4] electrodeposition on fugitive scaffolds,[5] or electrochemical deposition accompanying hydrogen evolution,[6] dealloying of copper alloys,[7] and freeze-drying.[2]

Freeze-drying or casting was first used to manufacture ceramics with complex shapes of pores.[8] Later, it has been also used to obtain porous metal structures despite the tendency of metal powders to rapidly settle in a suspension and oxidation when exposed to water. Nowadays, freeze-drying is actively applied to obtain titanium,[9,10] iron[11,12], and copper[2,13–15] foams. For freeze-drying, a powder is suspended in a liquid carrier which can be water or other solvents such as camphene, or *tert*-butyl alcohol. The freezing solidification of this suspension produces high aspect ratio dendrites of the frozen solvent, which reject and concentrate metal or ceramic powders into the interdendritic space. After complete solidification, a sublimation process is applied to remove the crystallized solvent. Freeze-dried slurries are characterized by the formation of mostly lamellar or needle-shaped pores, hollow prisms, plates, hoppers, sectored plates, and solid prisms can be also observed.[16]

The pore structure and total porosity depend on the powder solid content/solvent ratio, freezing temperature, freezing rate, and direction of freezing[8] which affect the specific surface area, strength, thermal and electrical conductivity of these foams. As, for example, Liu et al.[15] investigated the influence of the freezing temperature in a range from −10 to −50 °C on the microstructure and compression stress. The 0.2% yield strength in these foams decreased from 25.4 to 12.6 MPa with increasing porosity from 65% to 80% in the direction parallel to the freezing front. Park et al.[2] prepared copper foams with open porosity of 63% from aqueous copper dispersions characterized by a ductile compression behavior with a high yield strength, and energy absorption despite their highly porous lamellar architectures generated by freeze-drying.

The formation of a highly porous structure after freeze-drying increases the specific surface area of these foams, which can then be used as a template for active coatings. Therefore, a potential application of directional freeze-dried copper foams may be an anodic current collector in a lithium-ion battery or electrodes in super capacitors, fuel cells, and applications in catalytic fields.[1,2,17] Mao et al.[17] used a copper freeze-dried foam to develop a 3D high-performance self-supporting anode with ZnO/ZnCo$_2$O$_4$/Co$_3$O$_4$ coating for lithium-ion batteries with a high reversible capacity and an excellent rate capability.

Another possibility to create porous metal foams is the sponge replication technique, also called the Schwartzwalder process. Those foams are characterized by an open-cell structure and hollow struts due to the burnout of the reticulated polyurethane (PU) template.[18] In general, open-cell metal foams are relatively stable, have satisfying strength, and high porosity with a relatively large specific surface area. Those foams made by the

A. Sutygina, Dr. U. Betke, Prof. M. Scheffler
Institute for Materials and Joining Technology – Nonmetallic Inorganic Materials and Composites
Otto-von-Guericke-University Magdeburg
Große Steinernetischstraße 6, Magdeburg 39104, Germany
E-mail: alina.sutygina@ovgu.de

The ORCID identification number(s) for the author(s) of this article can be found under https://doi.org/10.1002/adem.202001516.

**ADVANCED
SCIENCE NEWS**

www.advancedsciencenews.com

**ADVANCED
ENGINEERING
MATERIALS**

www.aem-journal.com

sponge replication technique are very attractive for catalytic applications and heat exchanger systems.[19] The sponge replication technique has been already applied for the manufacturing of a titanium alloys foam,[20,21] Ti$_6$Al$_4$V,[22] an austenitic steel foam,[23] and aluminum foams.[24]

A combination of the sponge replication and freeze-drying techniques can further facilitate an increase in the strut porosity and the total surface area of foams due to an additional formation of lamellar pores within the foam´s struts. Schelm et al.[25] obtained an additional strut porosity in open-porous alumina foams by the combination of the sponge replication technique with the freeze-drying technique. The foams were characterized by a strut porosity between 50% and 60% and total porosity of 90%. The additional strut porosity significantly increased the specific surface area of these foams from 70 to 200 cm^2 g^{-1} compared to foams prepared by the sponge replication technique without freeze-drying. This combination of manufacturing methods may be attractive for metal foams in which a large specific surface area and highly porous struts are required. However, despite the widespread application of freeze-drying and sponge replication technique for the manufacturing of porous metal structures, the combination of sponge replication and freezing technique has never been applied for preparing highly porous metal foams with open strut pores. Based on previous results,[25] this novel manufacturing route can be attractive for the manufacturing of copper foams with a high specific surface area.

In this article, the manufacturing of hierarchical porous open-cell copper foams by a combination of sponge replication and freezing technique using PU templates and an aqueous copper dispersion is presented. The influences of additional freezing of foams and thermal processing conditions (temperature and atmosphere) on the strut microstructure, porosity, specific surface area, yield strength, absorbed energy, and thermal conductivity of the copper foams were investigated. Finally, the most relevant process–structure relations are discussed.

2. Experimental Section

2.1. Specimen Preparation

Copper powder supplied by Ecka Granules (ECKA Kupfer CH UF 10, Ranshofen, Austria) with a purity of 99.81% and an average particle size of ≈10 μm was used for the manufacturing of copper foams. Sample preparation was conducted in two ways: sponge replication technique and a combination of sponge replication technique and freeze-drying technique. A schematic manufacturing illustration of replica processed foams (RP foams) and combined replica/freeze-drying processed foams (RP/FP foams) is shown in **Figure 1**. For the preparation of RP foams, copper powder and a 10.7 wt% solution of a polyvinyl alcohol binder (1.2 wt%, Optapix PA 4 G, Zschimmer and Schwarz Chemie GmbH, Lahnstein, Germany) in distilled water were mixed. The final copper slurry contained 83 wt% of copper powder.

The slurry for RP/FP foams contained 73 wt% of copper powder. The aqueous solution was 1.5 g methyl cellulose (Tylose 3000 P, methylhydroxyethyl cellulose, Carl Roth GmbH þ Co, KG, Karlsruhe, Germany) dissolved in 25 ml of distilled water. Methyl cellulose was used as an additional thickener to adjust the viscosity of the suspension to a level suitable for RP/FP foams to prevent drainage off of the aqueous slurry from the PU foam after coating.

The copper slurries were mixed in a planetary centrifugal mixer (THINKY Mixer ARE-250, THINKY Corp. Tokyo, Japan) at 2000 rpm for 6 min. Then, PU templates were dipped into the slurries and excess slurry was removed manually. An open-cell PU foam with a linear cell count of 20 ppi with a geometric size of 15 mm × 15 mm × 20 mm (Koepp Schaum GmbH, Oestrich Winkel, Germany) was taken as a template for the sample preparation. The RP foams were dried for 24 h at room temperature in air. The RP/FP foams were frozen for 24 h at −20 °C to obtain ice dendrites from the water content of the slurry. After freezing, these specimens were freeze dried for 24 h in vacuum at 0.01 mbar at −50 °C in a freeze dryer (Gefriertrockenschrank BETA 1-16 LMC 2, Martin Christ Gefriertrocknungsanlagen GmbH, Osterode, Germany).

The next processing step for both types of specimens was the binder and PU burnout which was conducted in air at 250 °C for 3 h and at 500 °C for 3 h in a circulating air furnace (KU 40/ 04/ A, THERMCONCEPT Dr. Fischer GmbH, Bremen, Germany); the heating rate was set to 1 K min^{-1}. After that, the copper foams were thermally processed in a conventional tube furnace (alumina tube, HTRH 70-600/1800, Carbolite-Gero GmbH and Co. KG, Neuhausen, Germany) for 6 h in Ar/H$_2$ atmosphere with 2 vol% H$_2$ at 500 and 900 °C, respectively.
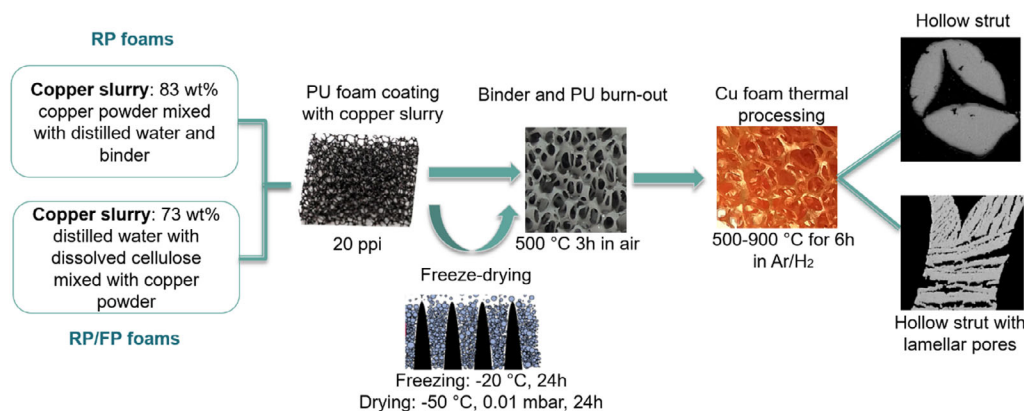

Figure 1. Schematic illustration of RP foams and RP/FP foams.

2.2. Characterization

A X'Pert Pro diffractometer (PANalytical GmbH, Kassel, Germany, Co $K\alpha_{1/2}$ radiation, 2θ, 40°–85°) with Bragg–Brentano reflection geometry was used for X-ray diffraction analysis (XRD). Rietveld analysis for the determination of the phase composition was conducted with the Topas Academic V5 software package.[26] The samples were prepared for measurements before the phase analyses: copper foams after binder and PU burning were milled and the obtained powder was loaded into backloading sample holders; the foams obtained after thermal processing were compressed to obtain a planar surface for a measurement in reflection geometry.

The measurements of the particle size distribution of the copper powder were conducted with a particle size analyzer Hydro2000SM (Malvern Instruments, Malvern, United Kingdom).

A thermal analyzer STA 449 F3 Jupiter (Netzsch-Gerätebau GmbH, Selb, Germany) was used to study the thermal transformation with respect to weight change and the oxidation behavior of the powder, which were analyzed with combined differential scanning calorimetry (DSC) and thermogravimetry (TG). The measurement range for the copper powder was from room temperature to 600 °C in air with a heating rate of 10 °C min⁻¹ and an air flow rate of 50 mL min⁻¹.

For the characterization of the copper powder morphology and the microstructure of cross sections of the thermally processed copper foams, a scanning electron microscope (SEM; FEI ESEM XL30 FEG, Hillsboro, OR/USA) was used. Prior to the microstructure characterization, the foams were vacuum impregnated in an epoxy resin, ground (180, 320, 600, 800, 1200, 2500, 4000 mesh grinding paper), and polished (diamond suspension 3 and 1 μm). Then, the foams were chemically etched in a solution of 100 ml of distilled water with 10 g ammonium peroxodisulfate, $(NH_4)_2S_2O_8$, for 30 s. Measurements of the average grain size were conducted using the ImageJ 1.48 s software (National Institutes of Health, USA).

An X-ray microcomputed tomograph (μ-CT, Phoenix Nanotom S, GE Sensing&Inspiration, Wunstorf, Germany) in a fast scan mode with an exposure time of 1000 ms per projection image was used for macrostructural analysis and for determining geometrical properties of the foam's macrostructure. Current and voltage of the X-ray tube were set to 50 μA and 100 kV for all measurements, respectively, and a 0.1 mm copper sheet was used as filter to avoid beam hardening artifacts. Selected single struts were cut from foams, then measured and reconstructed for calculating the strut wall thickness (D_{ws}), the thickness of material lamellae (D_{ml}), and the lamellar pore thickness (D_{lp}) (**Figure 2**). The pixel size was 3 μm to get a high resolution of the structure of the single struts. In addition, a complete foam was measured with a resolution of 7 μm to obtain strut thickness (D_s), cell and window size, and the ratio of the foam's surface area to the volume of the foam material ($Obj.S/Obj.V.$). The software package PhoenixDatos|X V2.0 (GE Sensing & Inspection Technologies GmbH, Wunstorf, Germany) was used to reconstruct the 3D sample volume from the collected radiographs.
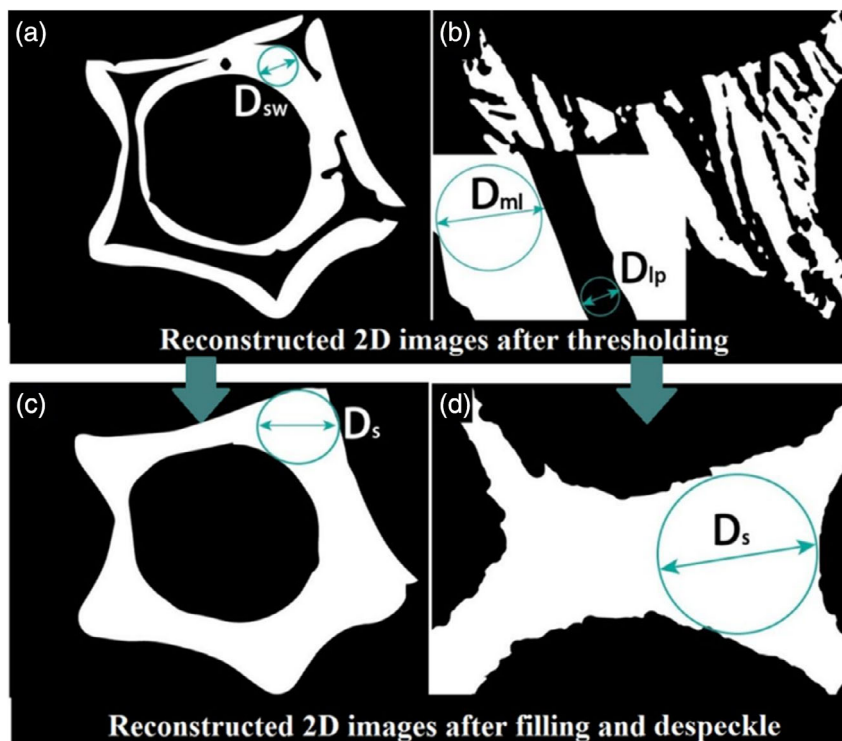

Figure 2. Illustration of a reconstructed 2D image: a,c) after thresholding; b,d) after filling and despeckle of the RP foam (left) and the RP/FP foam (right). A schematic of strut wall thickness (D_{sw}), thickness of material lamellae (D_{ml}), lamellar pore thickness (D_{lp}), and strut thickness (D_s) is included in the images.

The calculation of the material lamellae, lamellar pores, and structure thickness distribution was performed with the software package CTAnalyzer (CTAn V1.18, Skyscan/Bruker microCT, Kontich, Belgium). The adjustment of the CTAnalyzer data import and binarization steps preceding the actual morphological calculations were conducted by a differential thresholding technique as described in the study by Betke et al.[27] After finishing of the binarization, the threshold step was implemented, and the 3D analysis with the CTAnalyzer was conducted to calculate the foams' geometric parameters. Figure 2a,c show an illustration of a reconstructed 2D image after thresholding.

The foams were filled after thresholding in the 2D space using the closing function, which was called morphological operation, to calculate the macropore size (cell and window pores) or strut diameters (D_S). Figure 2b,d show the struts after filling. A round kernel type was applied with a radius of 10 pixels. Afterward, the despeckle operation was applied to remove the remaining cavities (e.g., air bubbles) with an area of up to 10 000 pixels. The foam surface area after thresholding, filling, and despeckle was determined to compare the influence of hollow strut and lamellar pores on the foam surface area ($Obj.S.$).

The calculation of the specific surface area per mass was conducted via the measured foam surface area by μ-CT and a material density of 8.7 g cm^{-3} determined from copper tablets prepared similarly to that of foams.

The total porosity was measured based on the calculation of the geometric foam density and the skeletal density of the strut material (V_{pores}/V_{foam})[28] (density of the pure copper bulk 8.96 g cm^{-3}[29]). The Archimedes method was used for the measurements of the strut porosity ($V_{strut\ pores}/V_{struts}$) with water as an infiltrating fluid according to the DIN EN 623-2:1993-11 standard procedure.[30] The copper foams were placed in an ultrasonic bath and sonicated to completely fill the foam pores with water. A small amount of surfactant was added to reduce the surface tension. After that, the weight of dry, buoyant, and wet foams was measured.

Compression strength testing was conducted with a TIRAtest 2825 testing machine (TIRA GmbH, Schalkau, Germany) with a load rate of 2 mm min^{-1}. The foams were placed between loading plates with 150 mm in diameter. For each sample series, ten foams were measured to calculate the compression yield strength (σ^*) and a two-parameter Weibull distribution.[31] For each series of samples, the calculations of the Weibull parameter m and the compression yield strength were determined with the software package Visual-XSel14.0 (CRGRAPH, Starnberg, Germany).

Measurements of the thermal conductivity were conducted with the transient plane source (TPS) technique using a TPS 2500 S (Hotdisk SE, Gothenburg, Sweden). The sensor, which was 9.868 mm in diameter, was placed in between two foams sanded previously.[32] The heating power was 200 mW for five measurements for 5 s per each measurement. The samples were turned, therefore all sides were measured and a total of 20 measurements were obtained. The sensor temperature changes were used for the calculation of the thermal conductivity.[33]

3. Results

3.1. As-Received Copper Powder

Figure 3 shows XRD patterns, a SEM image, and TG and DSC analyses of the copper starting powder. The initial copper powder, as-received from the supplier, did not consist of copper oxides or impurities, which may be detectable by XRD analysis, probably because their amount was below the detection limit of the XRD method, or copper oxides may be present in an amorphous state (Figure 3a). The powder particles had a nonspheroidal geometry and a flaky shape. From the particle size distribution of the powder, it follows that $d_{50} = 10.5 \pm 0.5$ μm with 10% of all particles <3.7 μm and 10% >64.6 μm.

The TG and DSC curves of the copper powder show a linear weight gain above ≈183 °C that was assigned to the onset of an oxidation reaction with the oxidation peak at ≈193 °C until the onset of the second oxidation reaction with the oxidation peak at ≈474 °C occurred (Figure 3c). Simultaneously, with the onset of the second exothermic reaction, the rate of the weight gain increased. The total weight gain was ≈24%, which is in good agreement with the quantitative oxidation of Cu to CuO (theoretical weight increase: 25.2 wt%). Thus, the DSC and TG results of the copper powder can be explained by the formation of CuO and Cu_2O according to the following chemical reactions[34]
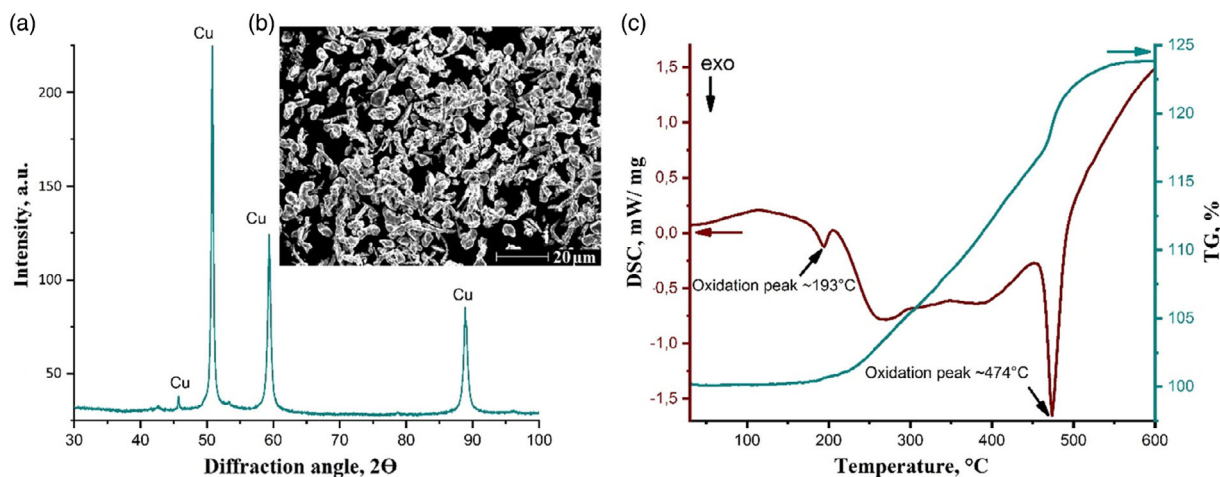

Figure 3. As-received copper powder: a) XRD patterns; b) SEM image; c) TG and DSC curves of the copper powder in air.
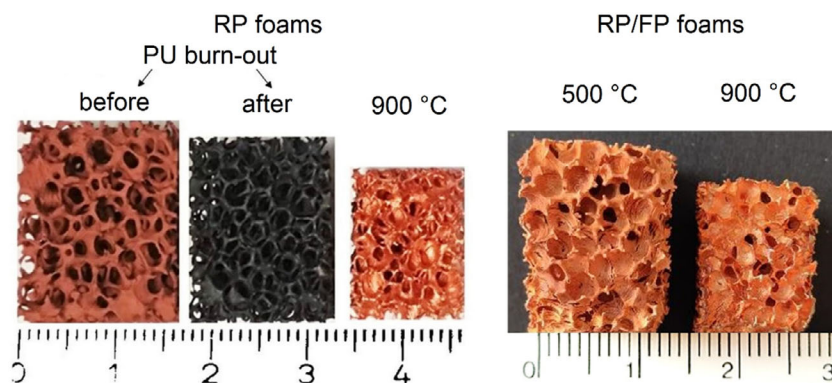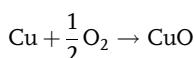
Figure 4. RP foams (left) and RP/FP foams (right).
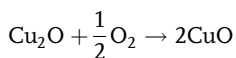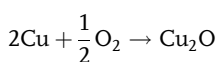
$$2Cu + \frac{1}{2}O_2 \rightarrow Cu_2O \qquad (1)$$

$$Cu_2O + \frac{1}{2}O_2 \rightarrow 2CuO \qquad (2)$$

$$Cu + \frac{1}{2}O_2 \rightarrow CuO \qquad (3)$$

In the study by Yabuki and Tanaka, [34] the formation of Cu_2O at the oxidation beginning of copper nanoparticles in 20% oxygen–nitrogen atmosphere was observed; a CuO phase was detected with increasing time and temperature of the experiment. In our case, the first oxidation peak was explained by the formation of Cu_2O and the second one was associated with the onset of CuO formation.

3.2. Compositional Change Before and After Thermal Processing

Figure 4 shows RP and RP/FP foams before and after PU burn-out and thermal processing for 6 h at 500 and 900 °C. The copper foams kept their shape after PU burnout; however, after this, the copper foams were of black color which was related to the copper oxidation due to PU removal in air. After further thermal processing in Ar/H_2, the RP foams had the typical copper color and were characterized by a high volumetric shrinkage in all directions (26% at 500 °C and 41% at 900 °C). Nevertheless, the copper foams kept its cellular structure.

After thermal processing at 900 °C, the copper RP/FP foams were characterized by higher shrinkage than the foams processed at 500 °C. The volumetric shrinkage was 23% after processing at 500 °C and 58% after processing at 900 °C related to the copper foam before PU burnout.

XRD patterns of the copper foams after PU burning and thermal processing at 500 and 900 °C are shown in **Figure 5**. From the XRD analysis it follows that, during the binder and PU burnout, the copper foams are oxidized to an amount of ≈50 wt% CuO and ≈50% Cu_2O wt% (Figure 5a). A pure copper phase was identified in all samples after further thermal processing in Ar/H_2 atmosphere. The chemical reduction of copper oxides with H_2 is expressed by the following reaction equations[35]

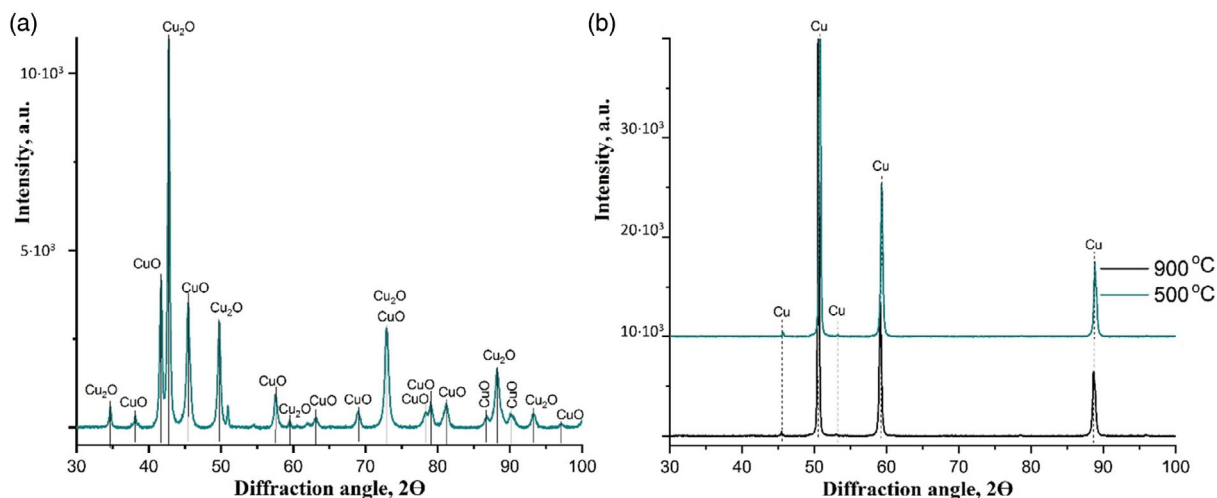$$Cu_2O + H_2 \rightarrow 2Cu + H_2O \qquad (4)$$

Figure 5. XRD patterns of the RP foams: a) after PU burnout at 500 °C for 3 h in air; b) after PU burnout and thermal processing for 6 h at 500 and 900 °C in Ar/H_2.

2001516 (5 of 12)

**ADVANCED
SCIENCE NEWS**

www.advancedsciencenews.com

**ADVANCED
ENGINEERING
MATERIALS**

www.aem-journal.com

$$CuO + H_2 \rightarrow Cu + H_2O \tag{5}$$

In the study by Park et al.,[2] a complete reduction of the cupric oxide powders was observed after sintering for 6–8 h; these samples were reduction preheat treated at 250 °C for 2 h under flowing Ar/H$_2$ atmosphere.

3.3. Microstructure

Figure 6 shows SEM cross-sectional images of RP foams before and after binder and PU burnout and thermal processing at 500 and 900 °C, respectively. The copper struts possess hollow cavities after PU burnout. The microstructure of the struts was porous after the binder and PU burnout (Figure 6b,g). Copper powder particles were more merged and densely packed in comparison with the green copper foams due to the oxidation of the copper powder particles in air (Figure 6a,f). Further thermal processing and chemical reduction of copper oxides in hydrogen atmosphere lead to a pronounced joining of the powder particles, a grain growth, a decrease in porosity, and pore rounding was observed (Figure 6c,h and d,i). After processing at 500 °C and etching of the samples, particle joining and grain formation was observed. This temperature, however, was not sufficient to compact the powder particles completely, therefore, the struts were still porous. Increase in the processing temperature to 900 °C lead to an increased number of joints between the powder particles, grain growth, and the formation of a homogeneous microstructure (Figure 6d,i). In comparison, the volumetric shrinkage reached 26% at 500 and 41% at 900 °C (**Table 1**). All the aforementioned changes in the microstructure are mainly related to the high temperature that was used during thermal processing which lead to grain growth, pore coalescence, reduction in porosity, and pore rounding due to enhancing atomic diffusion along grain boundaries, over the surfaces, and through the crystalline lattice.[36,37]

From a comparison of copper foams processed at 900 °C (Figure 6d,i and e,j), it was concluded that RP foams had an average grain size of ≈38 μm, and for RP/FP, it was ≈23 μm. It is assumed that lamellar pores throughout the struts in these foams influence the particle joining and the later grain growth.

SEM images of the strut surface and cross sections of RP/FP foams after thermal processing at 500 and 900 °C are shown in **Figure 7** and **8**. Pores generated via freeze processing are visible for all samples, having a lamellar structure typical for materials processed with aqueous slurries (Figure 7a,b and d,e). The freezing direction and orientation of the lamellar pores are randomly, which is between perpendicular and parallel to the strut surface (Figure 8a,b and d,e). This was related to the nondirectional freezing of the samples due to the random orientation of the structural elements of the foams. The samples were put on a plate in the freezing chamber where the freezing front was from the air around them and the template on which the coating system (formerly the slurry) was located. A similar pore orientation behavior was observed in the study by Schelm et al.[25] It is seen that the thickness of lamellar pores was higher after thermal processing at 500 °C (Figure 8a–c) than at 900 °C (Figure 8d–f). Processing at 900 °C led to a more pronounced joining of the powder particles, as a result, the copper particles were densely packed (Figure 7f and 8f), which, in turn, led to higher volume shrinkage of the foams from being 23% after processing at 500 °C and 58% after 900 °C (Table 1). Despite the significant increase in the shrinkage, the lamellar pores kept their shape and did not collapse.

3.4. Porosity, Pore Structure, and Specific Surface Area

The results of porosity measurements with the Archimedes method for RP foams show that the total porosity of the copper foams was 94.6% after processing at 500 °C and 93.2% after processing at 900 °C (Table 1). For the manufacturing of the foams, the same amount of the slurry was used; however, the total porosity was higher at 500 °C due to an increase in shrinkage with increasing temperature as a result of the powder particle joining.
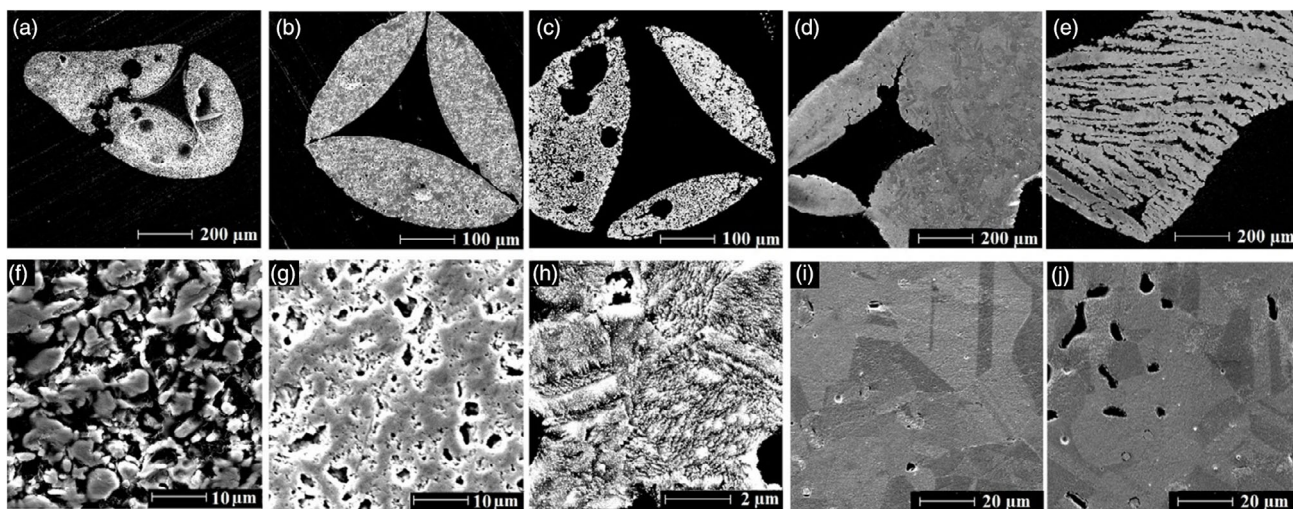

Figure 6. SEM images of RP foams: a,f) before binder and PU burnout; b,g) after binder and PU burnout; after processing for 6 h in Ar/H$_2$: c,h) at 500 °C RP foams; d,i) at 900 °C RP foams; e,j) at 900 °C RP/FP foams.

**ADVANCED
SCIENCE NEWS**

www.advancedsciencenews.com

**ADVANCED
ENGINEERING
MATERIALS**

www.aem-journal.com

Table 1. Geometrical, mechanical, and thermal properties of RP foams and RP/FP foams thermally processed for 6 h at 500 and 900 °C in Ar/H$_2$.

Sample	RP foams		RP/FP foams	
Thermal processing temperature [°C]	500	900	500	900
Volumetric shrinkage (S_v) [%]	26	41	23	58
Total porosity (P_{total})[a] [%]	94.6	93.2	93.1	87.7
Cell porosity (P_{cell})[b] [%]	87.7	89.7	76.7	68.3
Strut porosity (P_s)[c] [%]	49.5	28.7	60.3	55.7
Specific surface area by μ-CT [cm^2 g^{-1}]	–	25	–	47
Obj.S/Obj.V. [mm^{-1}]	–	22.1	–	41.2
Obj.S (after thresholding)/*Obj.S.* (after filling)	–	1.4	–	2.6
Mean diameter of struts [mm]	–	0.29 ± 0.22	–	0.46 ± 0.24
Mean cell size [mm]	–	2.4 ± 0.1	–	1.6 ± 0.3
Mean window size [mm]	–	1.9 ± 0.5	–	–
Yield strength [MPa]	0.12 ± 0.01	0.38 ± 0.06	0.10 ± 0.02	0.86 ± 0.20
Absorbed energy per volume [MJ m^{-3}]	0.05	0.10	0.14	0.39
Therm. Cond. of foam λ_f [W m^{-1} K^{-1}]	–	4.11 ± 0.23	–	4.95 ± 0.27
Therm. Cond. of porous strut material λ_s [W m^{-1} K^{-1}]	–	175.1	–	59.4
Bulk therm. Cond. of bulk material λ_b [W m^{-1} K^{-1}]	–	308.9	–	204.8

[a]($V_{material\ pores}$ + $V_{hollow\ strut\ pores}$ + $V_{cell\ pores}$)/V_{foam}; [b]including the cavities after PU template burnout ($V_{cell\ pores}$ + $V_{hollow\ strut\ pores}$)/V_{foam}; [c]related to the strut volume $V_{material\ pores}$/($V_{hollow\ strut\ pores}$ + $V_{material}$ + $V_{material\ pores}$).
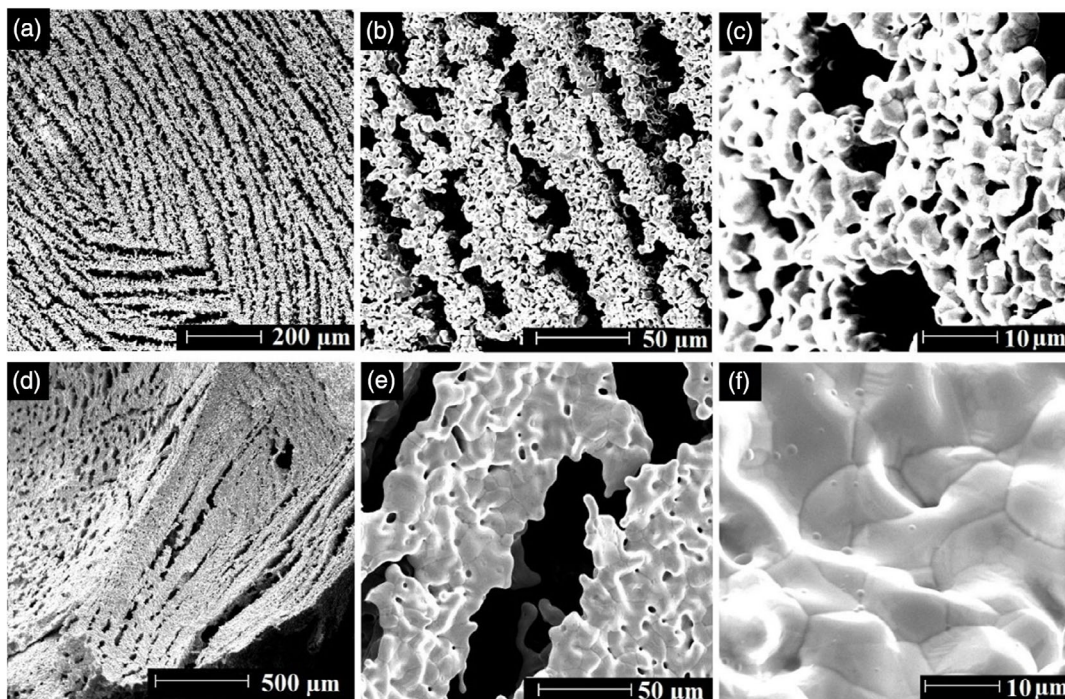

Figure 7. SEM images of RP/FP foams after thermal processing for 6 h in Ar/H$_2$: a–c) at 500 °C; d–f) at 900 °C.

Consequently, this decreased the strut porosity from ≈49.5% at 500 °C to ≈28.7% at 900 °C.

The RP/FP foams were also manufactured from the same amount of the slurry and after thermal processing at 900 °C foams showed a higher volumetric shrinkage (S_v ≈ 58%) and possess a lower total porosity (P_{total} ≈ 87.7%), cell (P_{cell} ≈ 68.3%) and strut porosity (P_s ≈ 55.7%) than the foams processed at 500 °C (S_v ≈ 23%, P_{total} ≈ 93.1%, P_{cell} ≈ 76.7%,

2001516 (7 of 12)

**ADVANCED
SCIENCE NEWS**
www.advancedsciencenews.com

**ADVANCED
ENGINEERING
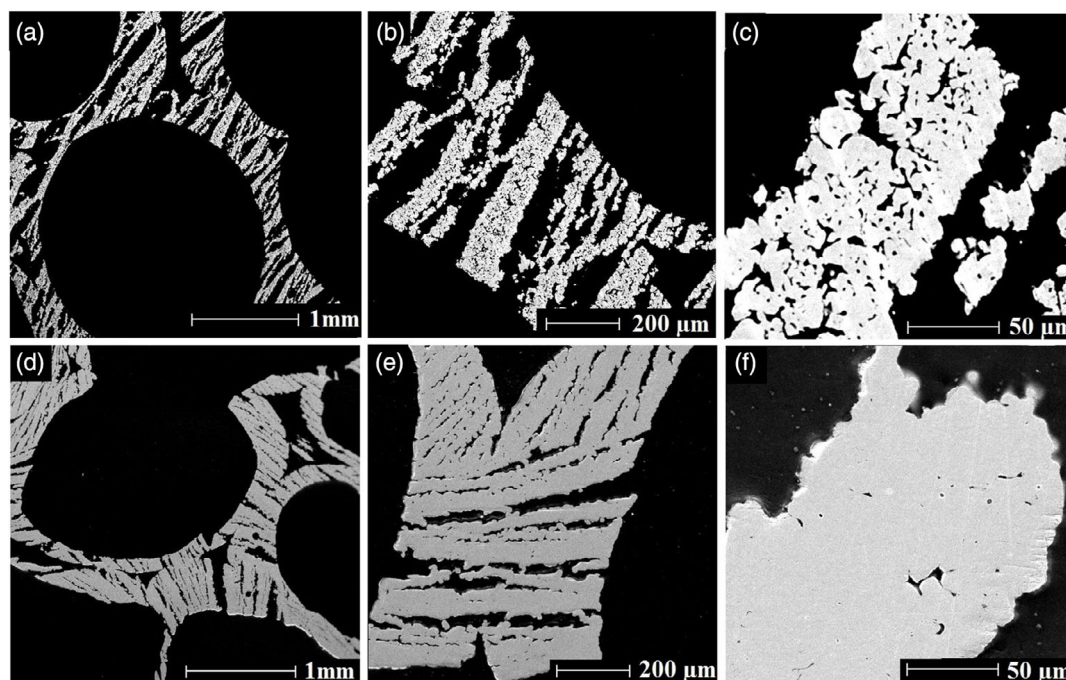MATERIALS**
www.aem-journal.com

Figure 8. SEM images of the cross section of RP/FP foams after thermal processing for 6 h in Ar/H$_2$: a–c) at 500 °C; d–f) at 900 °C.

$P_s \approx 60.3\%$). The aforementioned changes in porosity with increasing temperature cannot only be caused by increasing the particle joining of the copper powders with thermal processing temperature but also by additional shrinkage of the lamellar pores, which the struts are made of.

From the comparison of the RP foams and the RP/FP foams was reasoned that freezing of the copper foams significantly increased the strut porosity due to the formation of additional lamellar pores. For the foams processed at 500 °C, this value P_s changed from 49.5% to 60.3% and at 900 °C from 28.7% to 55.7%; in the latter case, it is almost doubled.

Figure 9 shows a μ-CT 3D reconstruction of the RP and RP/FP foams manufactured at 900 °C in Ar/H$_2$ for 6 h. The RP foams are characterized by open macropores such as cells and windows. The distribution of the macropore size and the strut thickness is shown in Figure 9c,d. The mean macropores size and strut thickness were determined by applying a Gaussian approximation to the distance histogram obtained from CTAnalyzer calculations of CT data, accordingly (Table 1). The mean window size of the RP foams was 1.9 ± 0.5 mm and the cell pore size was 2.4 ± 0.1 mm, the diameter of the struts $D_s \approx 0.29 \pm 0.22$ mm (after thresholding, filling, and despeckle). The mean size of the cells in RP/FP foams was 1.6 ± 0.3 mm and D_s was $\approx 0.46 \pm 0.24$ mm (after thresholding, filling and despeckle).

The μ-CT measurements of the strut wall thickness, material lamellae, and lamellar pore thickness distributions of the RP and RP/FP foams manufactured at 900 °C are shown in **Figure 10**. The mean diameter of D_{sw} of the RP foams was 130 ± 67 μm. The strut wall of the RP/FP foams consisted of material lamellae and lamellar pores; from the Gaussian approximation of the distance histograms obtained from the CTAnalyzer calculations, the mean diameter of D_{ml} was 72 ± 36 μm and 35 ± 21 μm for D_{lp}, respectively.

The formation of additional lamellar pores significantly increased the specific surface area (Table 1). The RP foams had 25 and 47 cm^2 g^{-1} was calculated for the RP/FP foams after processing at 900 °C. Consequently, the surface-to-volume ratio $Obj.S/Obj.V.$ increased by a factor of 1.9 after the formation of lamellar pores. For an estimation of the influence of inner hollow struts surface and lamellar pores on the total foams surface, the total surface areas $Obj.S$ were compared after thresholding and after filling. This ratio $Obj.S$ (after thresholding)/$Obj.S.$ (after filling) for the RP foams was 1.4 indicating a slight increase of the foams' surface due to the formation of hollow struts after PU burnout. The ratio $Obj.S$ (after thresholding)/$Obj.S.$ (after filling) for the RP/FP foams was 2.6 due to the additional surface area from lamellar and hollow strut pores.

3.5. Mechanical Strength

The compression strength test showed that the average yield strength value σ^* was 0.12 ± 0.01 MPa for the RP foams manufactured at 500 °C and 0.38 ± 0.06 MPa at 900 °C with a calculated Weibull parameter m for each sample series being 11.4 and 6.6, respectively. **Figure 11**a shows the compression strength behavior of the RP foams. From the shape of the curves, it was observed that the stress–strain behavior in the initial compression stage had an elastic deformation region characterized by a linear increase in stress–strain until exceeding the yield strength point. The stress–strain curve changed its behavior at the yield strength point, which was the onset of plastic deformation of cell walls. Further curse of stress–strain curves was characterized by long plateau regions (plastic cell collapse)[38] with a slow stress increase. The increase in yield strength was associated with a decrease in the strut porosity caused by processing at 900 °C.
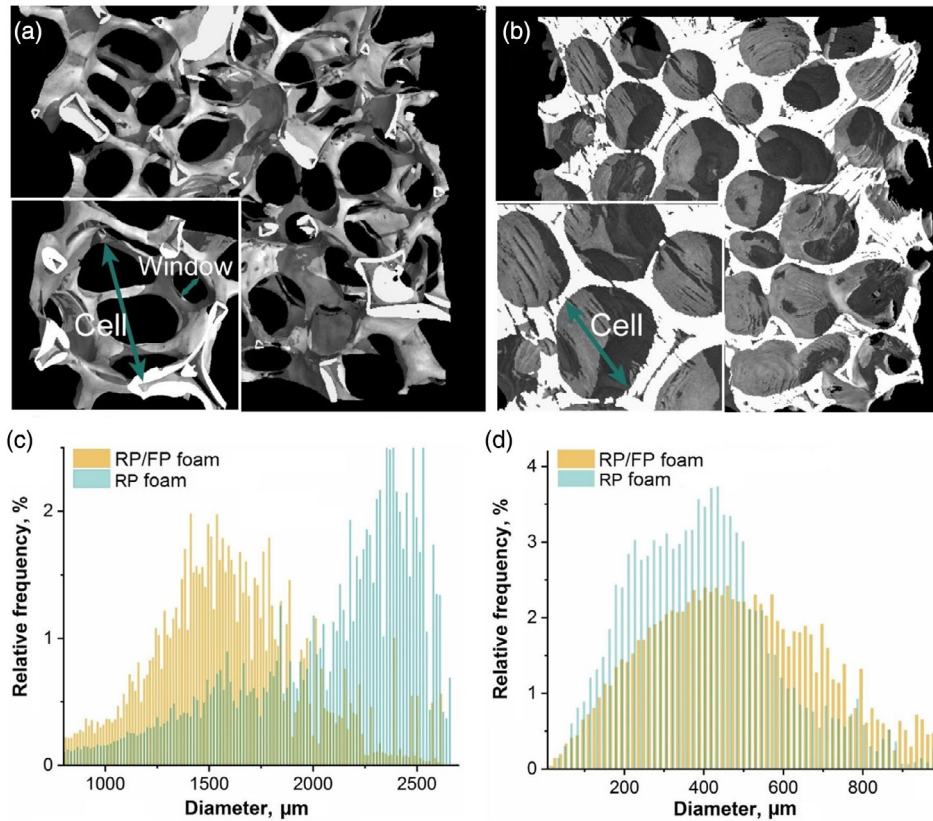
Figure 9. X-ray μ-CT reconstruction image of the RP and RP/FP foams after processing at 900 °C in Ar/H$_2$ for 6 h: a) RP foams; b) RP/FP foams; c) cell size distribution (cell and windows); d) strut thickness (D_s) distribution from a 3D μ-CT reconstruction after thresholding, filling, and despeckle.
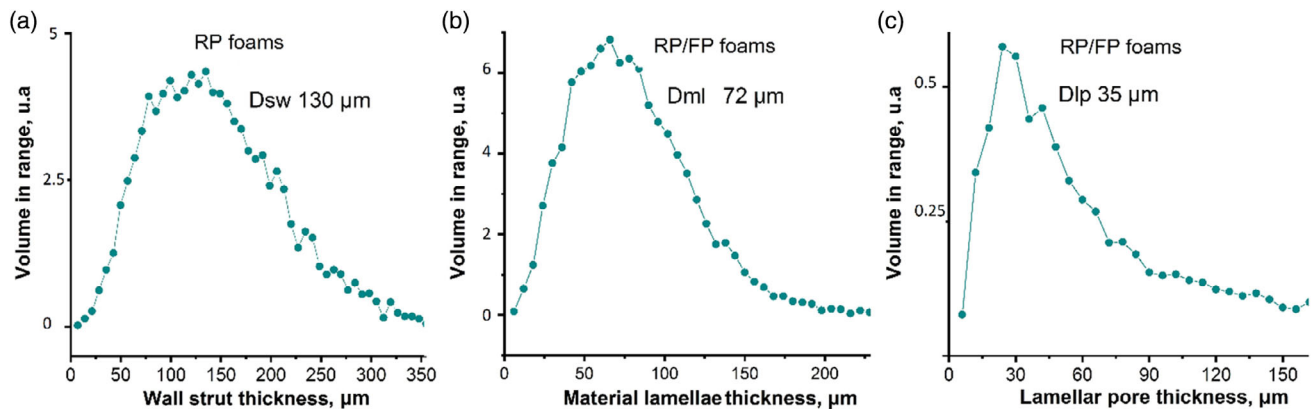

Figure 10. μ-CT measurements of the foams after processing at 900 °C in Ar/H$_2$ for 6 h: a) distributions of the strut wall thickness (D_{sw}) of the RP foams; b,c) material lamellae thickness and lamellar pore thickness of the RP/FP foams.

The stress–strain curve behavior of the RP/FP foams processed at 900 °C was characterized by intensive strength increase with strain in comparison with the foams processed at 500 °C (Figure 11b). The average yield strength value σ^* was 0.10 ± 0.02 MPa ($m = 4.2$) for the foams processed at 500 °C and 0.86 ± 0.20 MPa ($m = 4.6$) at 900 °C.

The energy absorption of the copper foams was determined from the integrated area under the stress–strain curve according to Equation (6)[38]

$$W = \int_0^{\varepsilon_D} \sigma(\varepsilon)\mathrm{d}\varepsilon \tag{6}$$

where W is the energy absorption per unit volume and ε_D is the densification strain. Figure 11a schematically shows the definition of ε_D. The densification strain was defined as the strain corresponding to the end of the stress plateau at which opposing cell walls start to come into contact and crush together.[39] The stress plateau region is characterized by the cells, which collapse as a
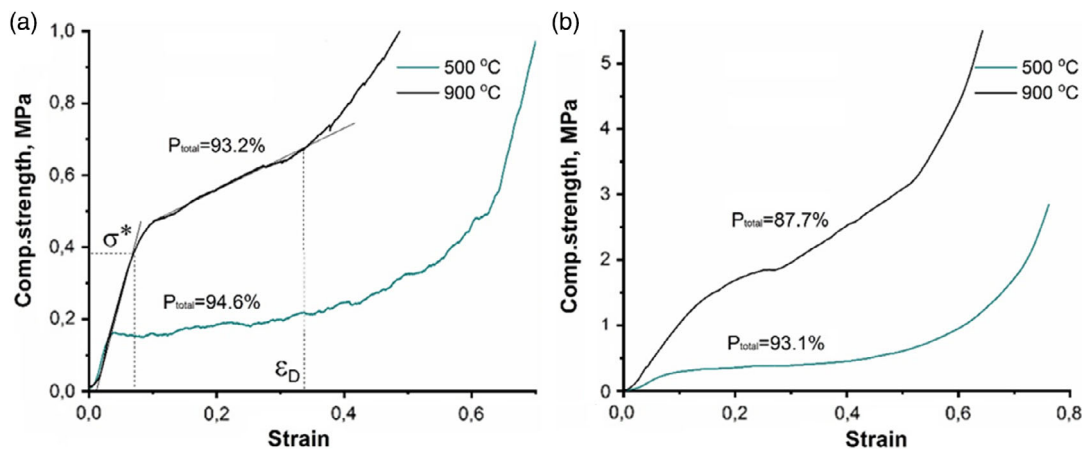
**ADVANCED
SCIENCE NEWS**

www.advancedsciencenews.com

**ADVANCED
ENGINEERING
MATERIALS**

www.aem-journal.com

Figure 11. Compression stress–strain curves: a) RP foams; b) RP/FP foams; where σ^* is the yield strength and ϵ_D is the densification strain.

result of yielding, buckling, or cell crushing.[38] From the calculated absorbed energy shown in Table 1, it became evident that the absorbed energy increased not only with an increasing processing temperature from 0.05 MJ m^{-3} at 500 °C ($P_{total} \approx 94.6\%$) to 0.10 MJ m^{-3} at 900 °C ($P_{total} \approx 93.2\%$) for the RP foams but also with additional lamellar pores from 0.14 MJ m^{-3} at 500 °C ($P_{total} \approx 93.1\%$) to 0.39 MJ m^{-3} at 900 °C ($P_{total} \approx 87.7\%$) for the RP/FP foams.

One of the assumptions for the highest absorbed energy and yield strength at 900 °C for RP/FP foams may be associated with the lowest value of the total porosity in comparison with the reticulated-only foams, since it is known that stress and absorbed energy increase with a decreasing total foam porosity. Furthermore, an increase in strength may be related to the architecture of the pores. The direction and size of the lamellar pores influence on the compression strength, which growths with an increase in the orientation of the lamellae with respect to the loading direction.[2] However, in our case, the lamellar pores had an anisotropic orientation with respect to the loading direction that may enhance the strength characteristics despite the high strut porosity ($P_s \approx 55.7\%$) via a load sharing mechanism.[40] A further systematic study is required to identify the relative importance of the above mechanisms.

3.6. Thermal Conductivity

The measurement of the thermal conductivity λ_f of RP and RP/FP foams manufactured at 900 °C was 4.11 ± 0.23 and 4.95 ± 0.27 W m^{-1} K^{-1}, respectively (Table 1). From the results, it is evident that the thermal conductivity of the foams is significantly lower than the thermal conductivity of the bulk copper, which is ≈ 413 W m^{-1} K^{-1}, which is connected with the negative influence of the cell and strut porosity on the thermal conductivity. For better comparison between the RP and RP/FP foams, thermal conductivity calculations were performed according to a model from Ashby[41] given in Equation (7) for the porous strut material, excluded the porosity within the struts[42,43]

$$\lambda_s = \frac{\lambda_f - P_{cell} \cdot \lambda_g}{1/3 \cdot (1 - P_{cell})} \tag{7}$$

In this equation, λ_g is the thermal conductivity of the gas phase (air) which is 0.0264 W·m^{-1} K^{-1},[41] P_{cell} is the cell porosity. The calculated strut thermal conductivity λ_s is shown in Table 1. The thermal conductivity of the porous strut material was $\lambda_s = 175.1$ W m^{-1} K^{-1} for the RP foams, and $\lambda_s = 59.4$ W m^{-1} K^{-1} for the RP/FP samples. The values of λ_s show, how the thermal conductivity decreased with an increase in the strut porosity of the foams.

A model derived by Eucken, see Equation (8), was used to estimate the thermal conductivity of the bulk strut material λ_b[44] from the thermal conductivity of the porous strut material calculated with Equation (7) and the strut porosity data obtained by the Archimedes measurements for both, RP and RP/FP foams

$$\lambda_s = \lambda_b \frac{1 + 2P_s \cdot \left(1 - \frac{\lambda_g}{\lambda_b}\right) \Big/ \left(2\frac{\lambda_g}{\lambda_b} + 1\right)}{1 - 2P_s \cdot \left(1 - \frac{\lambda_g}{\lambda_b}\right) \Big/ \left(2\frac{\lambda_g}{\lambda_b} + 1\right)} \tag{8}$$

In Equation (8), P_s is the strut porosity excluding the hollow strut cavities (Table 1) and λ_s is the thermal conductivity of the porous strut material taken from Equation (7). From the results shown in Table 1, it follows that with increasing the strut porosity, the λ_b decreases from 308.9 W m^{-1} K^{-1} for RP foams to 204.8 W m^{-1} K^{-1} for the RP/FP foams. This difference can be explained by an increase in the number of grain boundaries in the heat flow path with a decrease in the grain size. The low λ_b values for both foams compared to the pure bulk copper thermal conductivity (≈ 413 W m^{-1} K^{-1}) may also be associated with residual copper oxide(s) not been detected by XRD due to a concentration below the detection limit; from literature, it is known that copper oxides have low thermal conductivities ($CuO \approx 76.5$ W m^{-1} K^{-1}[45]; $Cu_2O \approx 4.5$ W m^{-1} K^{-1}[46]).

Compared to other convective methods of manufacturing porous copper foams, such as electrodeposition,[47] freeze-casting,[2,15,48] or lost carbonate sintering[4,49] the obtained RP/FP copper foams are characterized not only by high total porosity

(87–95%) but also high amount of open strut porosity (55–60%). This open strut porosity results in an increase in the specific surface area by a factor of 2 compared to conventional cellular metals. In addition, a structure containing comparatively large foam cells (mm range) plus highly porous struts is formed. Due to these large voids within the cellular structure compared to porous metals manufactured by freeze-casting, electrodeposition, or lost carbonate sintering, this gives a clear advantage with respect to the pressure drop characteristics for flowing fluid media. In summary, a porous structure with a low pressure drop and an increased specific surface area is formed, which is highly promising for applications in the field of catalyst supports or heat storage/pumping materials (after coating the foam surface with a catalyst or microporous adsorbent, respectively). Furthermore, unlike the conventional freeze casting method,[2,15,48] in which pores are formed along a suspension in a mold, the RP/FP foams have lamellar pores into struts of open-cell foams. In addition, these lamellar pores open the hollow strut cavities which cannot be obtained by the conventional sponge replication technique[18] or electrodeposition.[47] Despite the presence of the additional lamellar pores, the RP/FP foams thermally processed at 900 °C were characterized by high mechanical properties. Since the yield strength and absorbed energy are highly dependent on the total porosity, it is quite difficult to compare the RP/FP foams with foams obtained by other traditional manufacturing methods, due to the different porosity.

4. Conclusion

Copper foams with additional strut porosity were manufactured by a combination of sponge replication and freezing technique with subsequent sublimation removal of the water ice crystals. Their properties were compared to copper foams processed by sponge replication only without freeze processing. Copper foams processed at 500 and 900 °C for 6 h in hydrogen-containing atmosphere had a total porosity between 87% and 95%. It was observed that the processing temperature plays a critical role: increasing this temperature improved the particle joining process resulting in a higher connectivity, grain growth, but also reduction of the material strut porosity that improved the foams´ yield strength and absorbed energy. Therefore, foams manufactured at 900 °C are more attractive for further investigations.

The RP/FP foams were characterized by a high degree of additional strut porosity between 55% and 60% with randomly oriented lamellar pores. It was shown that the RP/FP foams increased the specific surface area by ≈1.9 times compared to the RP foams. The RP/FP foams possess a higher yield strength, energy absorption capability, and thermal conductivity than the RP foams. Thus, those type of copper foams may be attractive for support materials in the field of heterogeneous catalysis or heat exchanger applications where the specific surface area is important, or for high load with active materials.

Acknowledgements

Conflict of Interest

The authors declare no conflict of interest.

Data Availability Statement

Research data are not shared.

Keywords

[1] J. H. Um, H. Park, Y. H. Cho, M. P. B. Glazer, D. C. Dunand, H. Choe, Y. E. Sung, *RSC Adv.* **2014**, *4*, 58059.

[2] H. Park, M. Choi, H. Choe, D. C. Dunand, *Mater. Sci. Eng. A* **2017**, *679*, 435.

[3] Y. Yu, H. Wang, H. Zhang, Y. Tan, Y. Wang, K. Song, B. Yang, L. Yuan, X. Shen, X. Hu, *Electrochim. Acta* **2020**, *334*, 135559.

[4] Y. Y. Zhao, T. Fung, L. P. Zhang, F. L. Zhang, *Scr. Mater.* **2005**, *52*, 295.

[5] H. Park, C. Ahn, H. Jo, M. Choi, D. S. Kim, D. K. Kim, S. Jeon, H. Choe, *Mater. Lett.* **2014**, *129*, 174.

[6] H. C. Shin, J. Dong, M. Liu, *Adv. Mater.* **2003**, *15*, 1610.

[7] L. Zou, F. Chen, X. Chen, Y. Lin, Q. Shen, E. J. Lavernia, L. Zhang, *J. Alloys Compd.* **2016**, *689*, 6.

[8] S. Deville, *Adv. Eng. Mater.* **2008**, *10*, 155.

[9] Y. Chino, D. C. Dunand, *Acta Mater.* **2008**, *56*, 105.

[10] P. Trueba, A. M. Beltrán, J. M. Bayo, J. A. Rodríguez-ortiz, D. F. Larios, E. Alonso, D. C. Dunand, Y. Torres, *Metals (Basel)* **2020**, *10*, 188.

[11] R. Sepúlveda, A. A. Plunk, D. C. Dunand, *Mater. Lett.* **2015**, *142*, 56.

[12] S. K. Wilke, D. C. Dunand, *J. Power Sources* **2020**, *448*.

[13] S. T. Oh, S. Y. Chang, M. J. Suk, *Trans. Nonferrous Met. Soc. China* **2012**, *22*, s688.

[14] A. I. Cuba Ramos, D. C. Dunand, *Metals (Basel)* **2012**, *2*, 265.

[15] X. Liu, J. Wu, B. Luo, L. Zhang, Y. Lai, *Mater. Lett.* **2017**, *205*, 249.

[16] S. Deville, *J. Mater. Res.* **2013**, *28*, 2202.

[17] H. Mao, P. Shen, G. Yang, L. Zhao, X. Qiu, H. Wang, Q. Jiang, *J. Mater. Sci.* **2020**, 11.

[18] S. Singh, N. Bhatnagar, *J. Porous Mater.* **2018**, *25*, 537.

[19] A. Gancarczyk, K. Sindera, M. Iwaniszyn, M. Piatek, W. Macek, P. J. Jodłowski, S. Wroński, M. Sitarz, J. Łojewska, A. Kołodziej, *Catalysts* **2019**, 9.

[20] A. Manonukul, P. Srikudvien, M. Tange, C. Puncreobutr, *Mater. Sci. Eng. A* **2016**, *655*, 388.

[21] C. Wang, H. Chen, X. Zhu, Z. Xiao, K. Zhang, X. Zhang, *Mater. Sci. Eng. C* **2017**, *70*, 1192.

[22] J. P. Li, S. H. Li, C. A. Van Blitterswijk, K. De Groot, *J. Biomed. Mater. Res. – Part A* **2005**, *73*, 223.

[23] H. I. Bakan, K. Korkmaz, *Mater. Des.* **2015**, *83*, 154.

[24] A. Sutygina, U. Betke, M. Scheffler, *Materials (Basel)* **2019**, *12*, 3840.

[25] K. Schelm, T. Fey, K. Dammler, U. Betke, M. Scheffler, *Adv. Eng. Mater.* **2019**, *21*, 1.

[26] A. A. Coelho, *Topas Academic V5; Coelho Software*, Brisbane, Australia, **2012**.

[27] U. Betke, S. Dalicho, S. Rannabauer, A. Lieb, F. Scheffler, M. Scheffler, *Adv. Eng. Mater.* **2017**, *19*, 1700138.

[28] J. Henon, A. Alzina, J. Absi, D. S. Smith, S. Rossignol, *J. Porous Mater.* **2013**, *20*, 37.

[29] R. B. Ross, *Metallic Materials Specification Handbook*, Chapman & Hall, London, UK **1992**.

[30] Hochleistungskeramik, Monolithische Keramik, Allgemeine und strukturelle Eigenschaften, Teil 2: Bestimmung von Dichte und Porosität, *DIN EN 623–2:1993–11*, Beuth Verlag, Berlin, Germany, **1993**.

[31] W. Weibull, *J. Appl. Mech.* **1951**, *13*, 293–297.

[32] T. Log, S. E. Gustafsson, *Fire Mater.* **1995**, *19*, 43.

[33] Y. He, Thermochim. *Acta* **2005**, *436*, 122.

[34] A. Yabuki, S. Tanaka, *Mater. Res. Bull.* **2011**, *46*, 2323.

[35] M. M. Mahmoud, G. Link, M. Thumm, *J. Alloys Compd.* **2015**, *627*, 231.

[36] G. N. Felege, N. P. Gurao, A. Upadhyaya, *Metall. Mater. Trans. A Phys. Metall. Mater. Sci.* **2019**, *50*, 4193.

[37] R. M. German, *Powder Metallurgy and Particulate Materals Processing*, Princeton **2005**.

[38] L. J. Gibson, M. F. Ashby, *Cellular Solids: Structure and Properties*, Cambridge university press, Cambridge, United Kingdom, **1999**.

[39] P. J. Tan, S. R. Reid, J. J. Harrigan, *Int. J. Solids Struct.* **2012**, *49*, 2744.

[40] N. Bekoz, E. Oktay, *Mater. Sci. Eng. A* **2013**, *576*, 82.

[41] M. F. Ashby, *Philos. Trans. R. Soc. A Math. Phys. Eng. Sci.* **2006**, *364*, 15.

[42] U. Betke, A. Lieb, F. Scheffler, M. Scheffler, *Adv. Eng. Mater.* **2017**, *19*, 1.

[43] A. Sutygina, U. Betke, M. Scheffler, *Adv. Eng. Mater.* **2020**, 24.

[44] A. Eucken, *Die Wärmeleitfähigkeit feuerfester Stoffe. Ihre Berechnung aus der Wärmeleitfähigkeit der Bestandteile*, VDI-Verlag, Berlin, Germany, **1932**.

[45] Y. J. Hwang, Y. C. Ahn, H. S. Shin, C. G. Lee, G. T. Kim, H. S. Park, J. K. Lee, *Curr. Appl. Phys.* **2006**, *6*, 1068.

[46] H. Timm, J. Janek, *Solid State Ionics* **2005**, *176*, 1131.

[47] J. Chen, S. Dai, C. Li, W. Li, Y. Ren, *Materials (Basel)* **2018**, *11*, 1639.

[48] S. K. Hyun, H. Nakajima, *Mater. Sci. Eng. A* **2003**, *340*, 258.

[49] X. Lu, Y. Zhao, G. Wang, X. Zhu, *Results Phys.* **2020**, *19*, 103655.